Energy Spectrum Correction and Carrier Mobility Calculation of CdZnTe Pixel Detector Based on the Depth of Interaction

Rui Wu, Yang Kang, Dengke Wei, Donghai Fan, Yingrui Li, Sen Wu, Jiangpeng Dong, Donglei Chen, Tingting Tan, and Gangqiang Zha

***Abstract*— An experimental method was described to calibrate the depth of interaction (DOI) of high-energy γ-ray in large-size thick pixel CdZnTe detector. The experimental results indicated that the ratio of the cathode and anode amplitude strongly showed linear relationship with the DOI of incidence γ-rays and the detector. The correlation coefficients were optimized. Based on the experimental calibration of DOI, the photoelectric effect signals from the depth range where the energy resolution and the photopeak location are high were screened out to draw the energy spectrum. In this way, the energy resolution of the CdZnTe pixel detector was improved to 0.707% for ^{137}Cs@662 keV. Further combined with the anode rise time, the electron mobility of CdZnTe in 2-D (1 mm accuracy) and 3-D (2 mm × 2 mm × 1 mm accuracy) scales was calculated. At different pixel positions and depths in CdZnTe detector, the electron mobility varies between 1000 and 1150 cm^2/(V·s).**

***Index Terms*— Carrier mobility, CdZnTe detector, depth of interaction (DOI), energy spectrum correction, gamma ray detector.**

I. Introduction

CdZnTe is widely considered a comprehensive and promising semiconductor in radiation detection and imaging [1]–[3]. For its high atomic number, high resistivity, and suitable bandgap, CdZnTe detector delivers good energy resolution, decent spatial resolution, and high detection efficiency and has been widely used in nuclear medicine [4], space applications [3], nuclear safety monitoring [5], and other fields.

Manuscript received 19 January 2022; revised 15 March 2022 and 16 April 2022; accepted 19 April 2022. Date of publication 26 April 2022; date of current version 18 July 2022. This work was supported in part by the National Natural Science Foundation of China under Grant 61874089, in part by the Guangdong Basic and Applied Basic Research Foundation under Grant 2021A1515012558, and in part by the Science, Technology and Innovation Commission of Shenzhen Municipality under Grant CJGJZD20210408091402006.

Rui Wu, Yang Kang, Dengke Wei, Donghai Fan, Yingrui Li, Sen Wu, Tingting Tan, and Gangqiang Zha are with the School of Materials Science and Engineering, Northwestern Polytechnical University, Xi'an 710072, China, and also with the Shenzhen Research Institute, Northwestern Polytechnical University, Shenzhen 518057, China (e-mail: wurui@mail.nwpu.edu.cn; zha_gq@nwpu.edu.cn).

Jiangpeng Dong is with the Northwest Institute of Nuclear Technology, Xi'an 710613, China (e-mail: dong_jp@foxmail.com).

Donglei Chen is with Shenzhen CGN Engineering Design Company, Ltd., Shenzhen 518124, China (e-mail: chendonglei@cgnpc.com.cn).

Color versions of one or more figures in this article are available at https://doi.org/10.1109/TNS.2022.3170427.

Digital Object Identifier 10.1109/TNS.2022.3170427

In CdZnTe, the holes are easily trapped, resulting in incomplete charge collection and low-energy tailing of the characteristic energy peak. The CdZnTe detector usually adopts the electrode design that collects a single polarity carrier [6]–[11] to reduce incomplete hole collection for imaging and high-energy γ-rays' detecting applications. Among them, pixel, grid pixel, and coplanar grid array electrodes are typical schemes that can obtain the 2-D interaction position on the anode plane by the triggered pixel. However, direct detection cannot get the depth of interaction (DOI) perpendicular to the electrodes. The DOI of γ-rays in the detector is significant for improving energy resolution, Compton imaging, and detecting high-energy γ-rays. The DOI information is obtained based on one-to-one correspondence between the DOI and the ratio of the cathode-to-anode signals. There are detailed theoretical derivations in [12]–[14]. Based on this, they further calculated the carrier mobility lifetime product [12], [15]. In [16], they calibrated the DOI using a simulation tool and considered using a linear function with an exponential term suitable for fitting the experimental results. In [17] and [18], they used electron signal rise time to correct the anode signal pulse height to make the induction signal measurement more accurate. The rise time correction makes sense for DOI because DOI is proportional to the signal rise time. This article designed a calibration experiment to calibrate the relationship between the DOI and the cathode and anode signals of the thick CdZnTe pixel detector with a simple function and studied the fitting parameters to optimize the depth reconstruction effect. Based on the analysis of DOI, the energy spectra of the CdZnTe pixel detector with high-energy γ-rays incident on the cathode in different depth layers were studied, and the method to improve the energy resolution was explored. Furthermore, a way to calculate the 3-D mobility of electrons in the crystal directly with DOI and carrier drift time was found.

II. Depth Calibration Experiment

When γ-ray incidents and deposits its energy in a CdZnTe pixel detector, the electron clouds generate and drift toward the electrode driven by the external electric field. As the 3-D interaction positions of the rays in the crystal are different, the electron cloud's drift path and diffusion degree vary accordingly. The amount of induced charge in the anode and

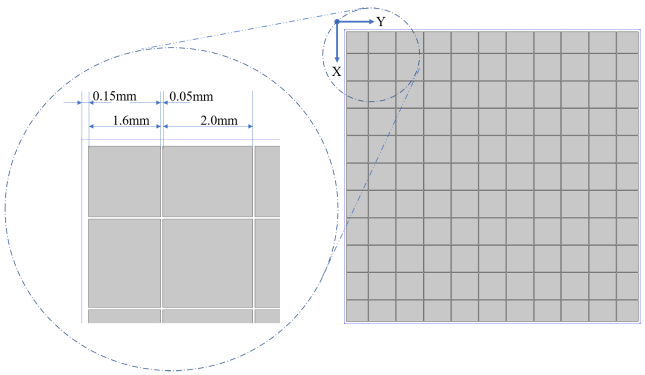

Fig. 1. Pixel arrangement and detailed size of the anode of the CdZnTe pixel detector.

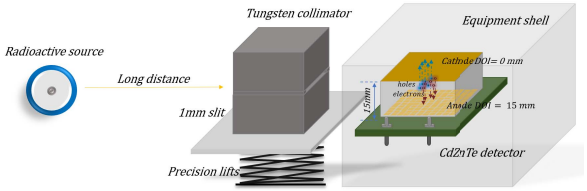

Fig. 2. Schematic of the depth calibration experiment.

cathode depends not only on the energy of the γ-ray but also on the 3-D interaction position. In addition, the crystal defects will also affect the amount of induced charge. It is necessary to study the characteristics of the induced signal at different depths and pixels to achieve better energy resolution. The scale of the studied CdZnTe pixel detector is 22 mm $\times$ 22 mm $\times$ 15 mm, of which the thickness is 15 mm, and the electrode area is 22 mm $\times$ 22 mm. The anode pixel arrangement is 11 $\times$ 11, and Fig. 1 shows the exact pixel size. The ORTEC 672 Spectroscopy Amplifier tests the induced signals of the cathode and anode. LeCroy Waverunner 610Zi oscilloscope measures the signal rise time of the preamplifier signals connected to the anode pixels.

The depth calibration experiment was designed to quantitatively analyze the relationship between the DOI of radiation and the amplitude of the anode and the cathode. Fig. 2 shows the experimental scheme. The two tungsten blocks can attenuate the intensity of the incident γ-rays by more than 95%, and the slit between them constrains the incident direction of the γ-ray so that γ-rays can only be incident in the direction parallel to the slit. The width of the slit determines the accuracy of depth calibration. It was 1 mm in this article. By adjusting the precision lifts, the upper surface of the collimating slit and the anode of the detector were made in the same plane. The collimation slit was adjusted to align to different depths on the side of the detector by adding 1-mm standard gauges. The dimensional tolerance of the gauge blocks is 0.0005 mm. Therefore, the height error of gauge blocks can be ignored.

To make the energy deposition uniform in each depth layer of the CdZnTe detector, ^{137}Cs and ^{60}Co were used as the radiation source for depth calibration. The plane with DOI = 0 mm

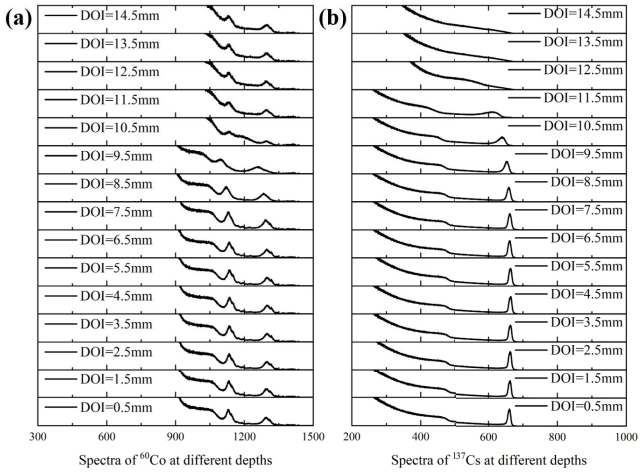

Fig. 3. Energy spectra response of the CdZnTe detector when γ-rays of (a) ^{60}Co and (b) ^{137}Cs are incidents at different depths, respectively.

is defined as the cathode plane and DOI = 15 mm is defined as the anode plane. The energy spectrum response of the CdZnTe detector when γ-rays of ^{60}Co and ^{137}Cs are incident at different depths is shown in Fig. 3. Each energy spectrum was obtained by adding up spectra from all active pixels.

In Fig. 3, the legends "DOI = x mm" represent the position of the center plane of the collimating slit. Fig. 3(a) shows the depth energy spectra of ^{60}Co, the photopeak near the anode and the cathode has a relatively high peak position and energy resolution. The photopeak positions shift to the left, and the energy resolution reduces slightly at a distance of 9–11 mm from the detector cathode. In Fig. 3(b), showing the depth energy, the peak positions of characteristic energy peak gradually shift to the left and widen between 10 and 15 mm, whereas for depth from 0 to 10 mm, there are slight changes in energy resolution and photopeak position. The reason for different trends of ^{60}Co and ^{137}Cs depth energy spectra when DOI $>$ 11 mm is due to the fact that the weighting potential starts to rise near the anode and the collimator has different attenuation degrees for the intensity of different energy rays.

III. Theory and Analysis

According to the Shockley–Ramo principle, the induced charge of the cathode or anode is related to the carrier charge and the weighting potential difference of the start and end positions. In semiconductor detectors, both electrons and holes will contribute to the cathode- and anode-induced signals which are calculated by (1) and (2), and the schematic is shown in Fig. 4

$$Q\text{anode} = -[e \times \Delta\varphi(e@\text{anode}) + h \times \Delta\varphi(h@\text{anode})] \quad (1)$$

$$Q\text{cathode} = -[e \times \Delta\varphi(e@\text{cathode}) + h \times \Delta\varphi(h@\text{cathode})]. \quad (2)$$

Among them, e and h are the charges carried by electrons and holes, respectively, in which e has a negative value and h has a positive value. $\Delta\varphi$ is the weighting potential difference between the beginning and end positions of the carriers. $\Delta\varphi(e@\text{anode})$ and $\Delta\varphi(e@\text{cathode})$ represent the

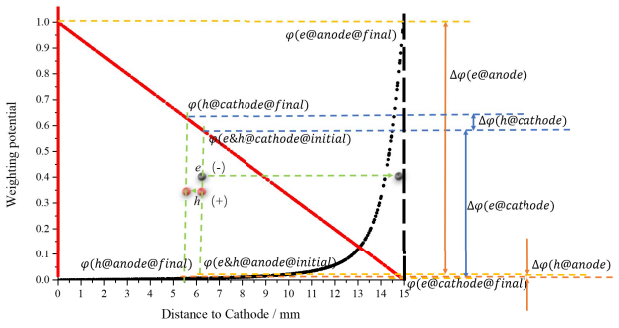

Fig. 4. Schematic of cathode and anode weight potential and induced signal.

change in the weighting potential of electrons at the anode and the cathode, respectively. $\Delta\varphi(h@\text{anode})$ and $\Delta\varphi(h@\text{cathode})$ represent the change in the weighting potential of holes at the anode and the cathode, respectively.

The trend in the depth energy spectra of ^{137}Cs can be explained. When the γ-ray deposits its energy near the anode, the differences in weighting potential between the start and end positions of the carrier drift distance are more prominent in the depth range of 1 mm, so the photopeak widens until there is no energy resolution ability.

To calculate the ratio of the cathode- and anode-induced signals generated by a photoelectric event, divide (2) by (1) and we get the following equation:

$$\frac{Q\text{cathode}}{Q\text{anode}} = \frac{[-e \times \Delta\varphi(e@\text{cathode}) + h \times \Delta\varphi(h@\text{cathode})]}{[-e \times \Delta\varphi(e@\text{anode}) + h \times \Delta\varphi(h@\text{anode})]}. \tag{3}$$

In the CdZnTe detector, the hole mobility lifetime product is about one-hundredth of the electrons. Therefore, the drift distance of the hole is relatively short, and the difference in weighting potential of hole drifting is relatively tiny compared with that of the electrons. The contribution of the hole to the cathode-induced signal and anode-induced signal is small and can be ignored. Discard the contribution of the hole in (3) and assume that the drifting ability of electrons is strong enough so that they can eventually drift to the anode. The formula will simplify to

$$\begin{aligned}\frac{Q\text{cathode}}{Q\text{anode}} &\approx \frac{[-e \times \Delta\varphi(e@\text{cathode})]}{[-e \times \Delta\varphi(e@\text{anode})]} \\ \frac{Q\text{cathode}}{Q\text{anode}} &\approx \frac{[\Delta\varphi(e@\text{cathode})]}{[\Delta\varphi(e@\text{anode})]} \\ \frac{Q\text{cathode}}{Q\text{anode}} &\approx \frac{[\varphi(e@\text{cathode@initial})]}{[1-\varphi(e@\text{anode@initial})]}.\end{aligned} \tag{4}$$

Among them, $\varphi(e@\text{cathode@initial})$ represents the weighting potential of the electron on the cathode where it generates. $\varphi(e@\text{anode@initial})$ represents the weighting potential of the electron on the anode where it generates. For the amplitude of the output of the shaping amplifier proportional to the amount of induced charge, cathode to anode ratio (CAR) is defined as (Qcathode/Qanode) and calculated with the amplitude of the shaping amplifier signal of the cathode and anode. The red line in Fig. 5 represents the CAR calculated using (4). It has a one-to-one correspondence with DOI.

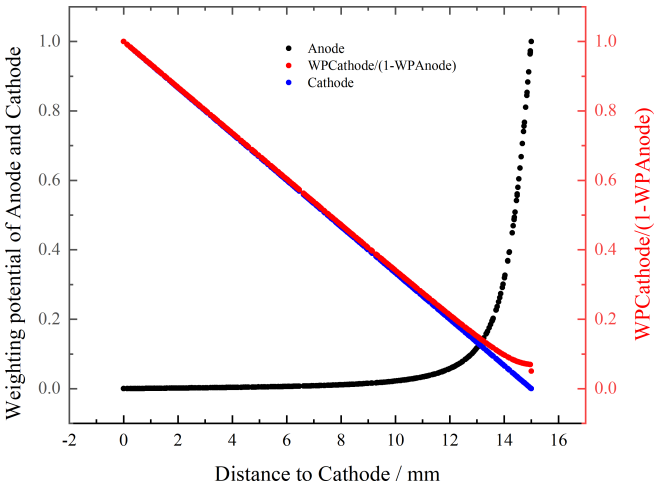

Fig. 5. Relationship between the weighting potential of the cathode and anode and the anode and cathode signal ratio.

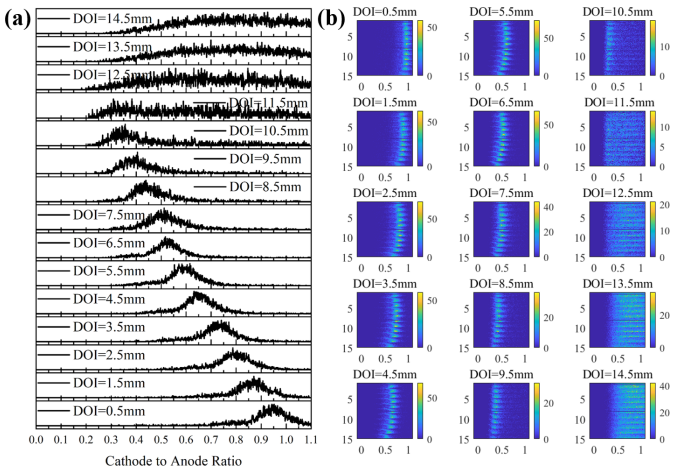

Fig. 6. CAR statistical distribution of (a) single pixel and (b) all pixels in different depths. The calibration source is ^{137}Cs.

Based on the above theoretical derivation, the events in the photopeak range of ^{137}Cs and ^{60}Co in Fig. 3 were used to calculate CAR and establish the relationship between DOI and CAR. Fig. 6 shows the calibration results of ^{137}Cs at different DOIs. Fig. 6(a) shows the CAR distribution of a single pixel, and Fig. 6(b) shows the CAR distribution of all pixels. The horizontal axis of each subgraph is CAR, and the vertical axis is DOI. The color from blue to yellow in Fig. 6(b) represents CAR counts at that position from less to more. Fig. 7 shows the calibration result of ^{60}Co. From Figs. 6(a) and 7(a), it can be found that within the depth range of DOI < 11 mm for a single pixel, the CAR distribution curve at each depth is Gaussian-like, and the peak value of the curve changes with DOI. In the depth range of DOI > 11 mm, the CAR values are distributed in a wide range independent of DOI. Figs. 6(b) and 7(b) also prove that CAR and DOI have a one-to-one correspondence when DOI < 11 mm for all pixels, and CAR cannot determine DOI when DOI > 11 mm. The possible reason for this phenomenon is as follows. The weighting potential slope of the cathode is

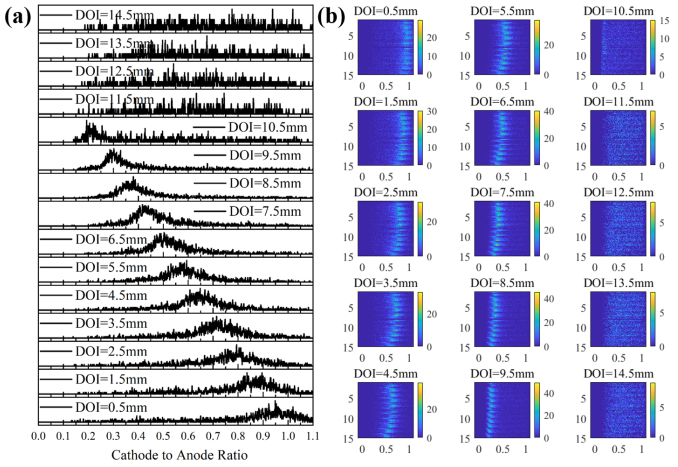

Fig. 7. CAR statistical distribution of (a) single pixel and (b) all pixels in different depths. The calibration source is ^{60}Co.

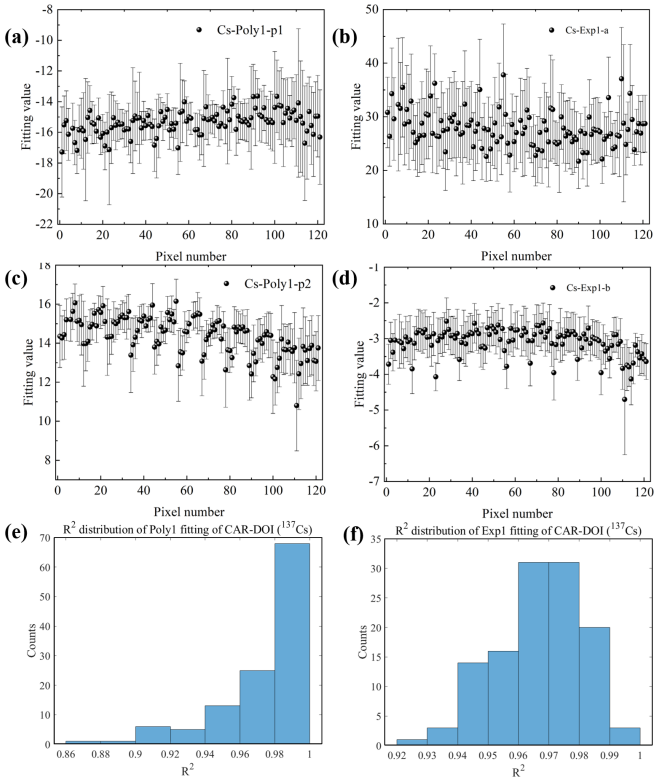

Fig. 8. Fitting result of CAR-DOI obtained by ^{137}Cs. (a), (c), and (e) Fitting parameters, the corresponding error bars, and R^2 distribution of linear fitting. (b), (d), and (f) Fitting parameters, the corresponding error bars, and R^2 distribution of exponential 1 fitting.

larger than the anodes in most crystal regions, and therefore, the cathode signal triggers the threshold. During experiment signal acquisition, the cathode signal is the trigger signal. Whereas in depths close to the anode, the slope of the anode weighting–potential curve increases rapidly. The anode signal generates before the cathode signal in the amplification system. But the cathode signal is still used as the trigger signal. Under this circumstance, the anode signal can be lost in whole or part, and CAR has nothing to do with DOI. The linear and first-order exponential function was used to fit the relationship between the DOI and the peak of the CAR distribution in the range of DOI <11 mm. The fitting function is as follows:

$$\text{Linear}: \text{DOI} = \text{slope} \times \text{CAR} + \text{intercept} \quad (5)$$

$$\text{Exponential 1}: \text{DOI} = a \times \exp(\text{CAR} \times b). \quad (6)$$

The fitting parameters, the corresponding error bars, and R^2 distribution obtained by ^{137}Cs and ^{60}Co are shown in Figs. 8 and 9, respectively.

To verify the theoretical calculation effect of each calibration parameter within the range of DOI >11 mm and the consistency of calibration parameters and theoretical parameters, the curve of DOI was calculated when CAR takes value from 0 to 1 and the average of all pixel fitting parameters. The corresponding DOI value is shown in Fig. 10. The calculated DOI value can better meet the actual situation (the crystal thickness is 15 mm) using the linear fitting parameters obtained from the ^{137}Cs calibration experiment. What is more, the intercept and slope of CAR-DOI calculated theoretically are -15.48571 and 15.38745, respectively, and the experimental results can also correspond well with it. The linear fitting parameters obtained from the ^{137}Cs calibration experiment were used to calculate the DOI in the following contents.

IV. Discussion

A. Energy Spectrum Correction Based on the DOI

The high-energy radioactive source ^{137}Cs was placed near the cathode of the detector to explore the energy spectrum characteristics of the detector at different depths and methods that can improve the energy resolution of the detector. Fig. 11(a) illustrates the energy deposition of ^{137}Cs@662 keV γ-ray through the photoelectric effect (only a pixel response at a time) at different thicknesses of the detector, where the horizontal axis is the ray energy, and the vertical axis is the DOI calculated by CAR. It is found that where DOI >11 mm, the closer the DOI to the anode, the lower the peak position and broader width of characteristic energy. Whereas when DOI <11 mm, the characteristic energy distribution is concentrated, and the Compton edge and the Compton backscattering peak are clear. Fig. 11(b) draws the energy spectrum at different depths using the scatter diagram in Fig. 11(a) with an accuracy of 1 mm in depth direction. The photopeak location and energy resolution of the energy spectrum in Fig. 11(b) are shown in Fig. 11(c) and (d), respectively. It is found that the photopeak position and energy resolution show superiority and then inferiority with increasing DOI. The highest peak position and the energy resolution appear in the central part of the detector. With the help of Fig. 4, the reason for performance changes in the depth energy spectrum can be illustrated. When γ-rays incident near the cathode, the drifting distance of the electron cloud is long and the degree of electron trapping is more significant. The weighting potential difference in electron drifting is close to 1 in this circumstance. Therefore, induced charge is only slightly lost, and photopeak is slightly lower. When the γ-rays incident on the central part of the detector, the drift

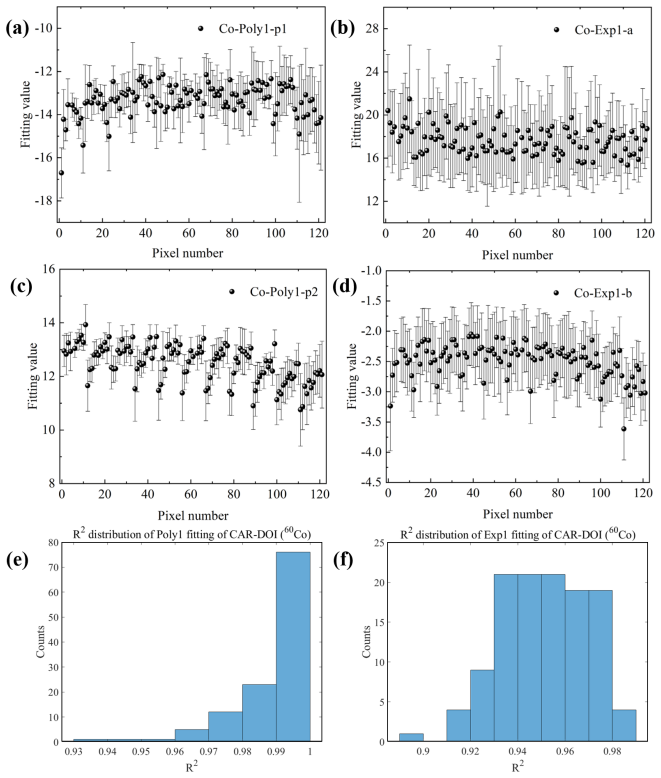

Fig. 9. Fitting result of CAR-DOI obtained by ^{60}Co. (a), (c), and (e) Fitting parameters, the corresponding error bars, and R^2 distribution of linear fitting. (b), (d), and (f) Fitting parameters, the corresponding error bars, and R^2 distribution of exponential 1 fitting.

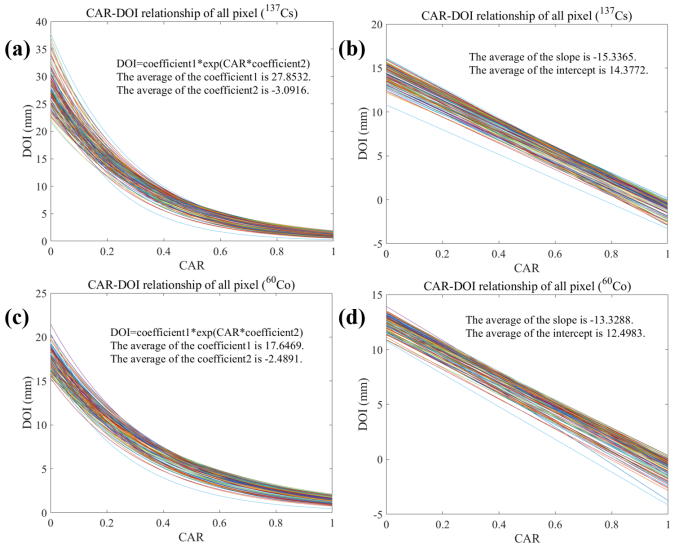

Fig. 10. DOI reconstruction of each pixel with four sets of fitting parameters: (a) exponential fitting of ^{137}Cs calibration data; (b) linear fitting of ^{137}Cs calibration data; (c) exponential fitting of ^{60}Co calibration data; and (d) linear fitting of ^{60}Co calibration data.

distance of the electron cloud is significantly short, with the weighting potential difference in electron drifting still close to 1. The theoretical yield of induced charge is large, and the charge loss is slight, so the photopeak is the largest here. When the γ-rays incident near the anode, the trapping of the electron cloud is minor, but the weighting of the anode has risen to a high level, and the weighting potential difference in electron drifting is significantly less than 1. The induced

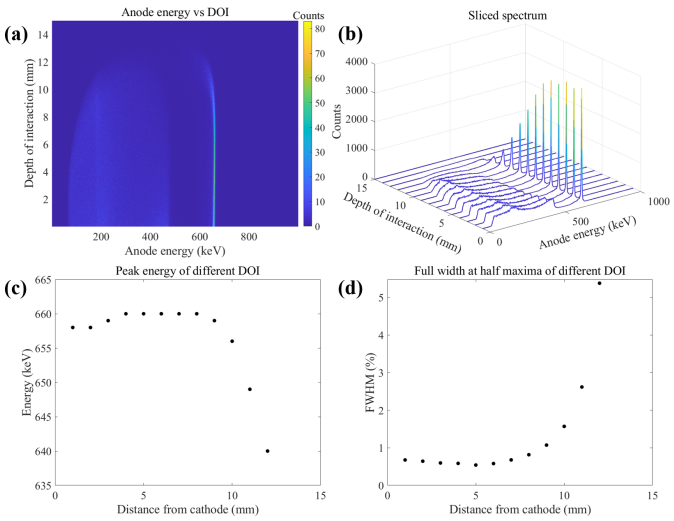

Fig. 11. Energy spectrum response of ^{137}Cs at different DOIs: (a) energy deposition of ^{137}Cs@662 keV γ-ray through the photoelectric effect. (b) Energy spectrum at different depths with an accuracy of 1 mm. The photopeak location and energy resolution of the energy spectrum in (b) are shown in (c) and (d), respectively.

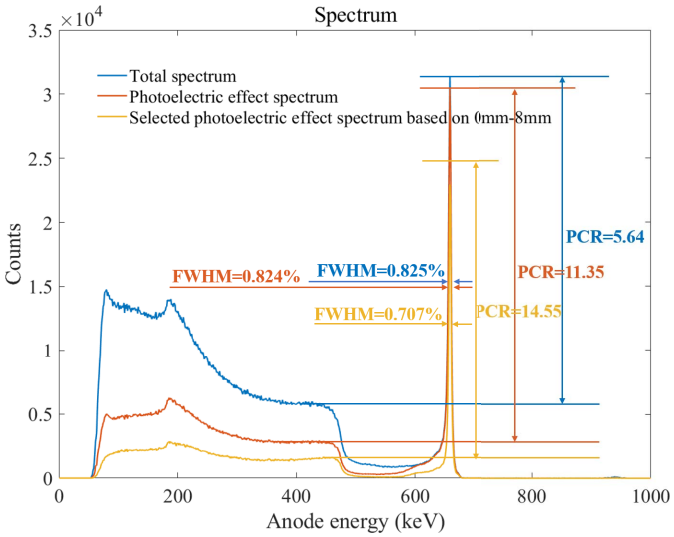

Fig. 12. Test energy spectrum (blue), photoelectric effect spectrum (red), and photoelectric effect spectrum with deep screening (yellow).

charge reduced considerably, and the photopeak position was also lower. From the degree of reduction of the photopeak position and energy resolution near the anode and cathode in (1) and (2), the conclusion is that the weighting potential difference in carrier drifting has a more significant influence on induced charge than carrier trapping.

Based on DOI calibration and the study of energy spectrum characteristics of detectors at different depths, a method was proposed to improve energy resolution. Choose the photoelectric effect events from depths where the energy resolution and photopeak position are high to form the energy spectrum. The data were not changed during screening retaining their originality and authenticity.

Fig. 12 shows comparison of the detector's test energy spectrum (blue), photoelectric effect energy spectrum (red),

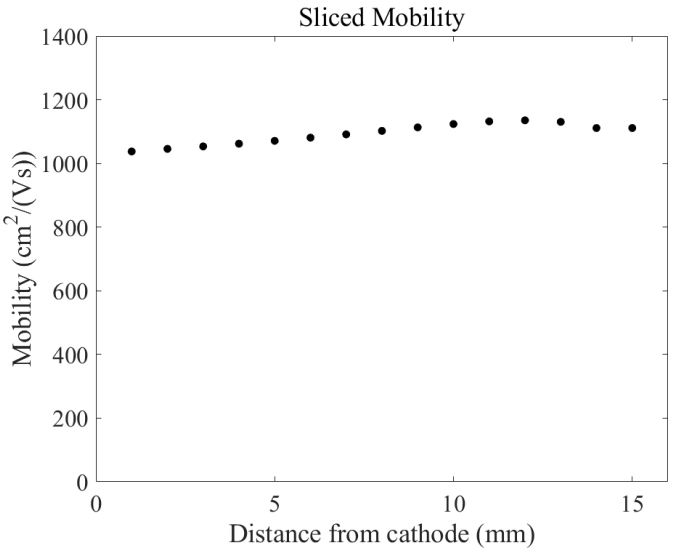

Fig. 13. 2-D electron mobility of the CdZnTe detector (depth accuracy is 1 mm).

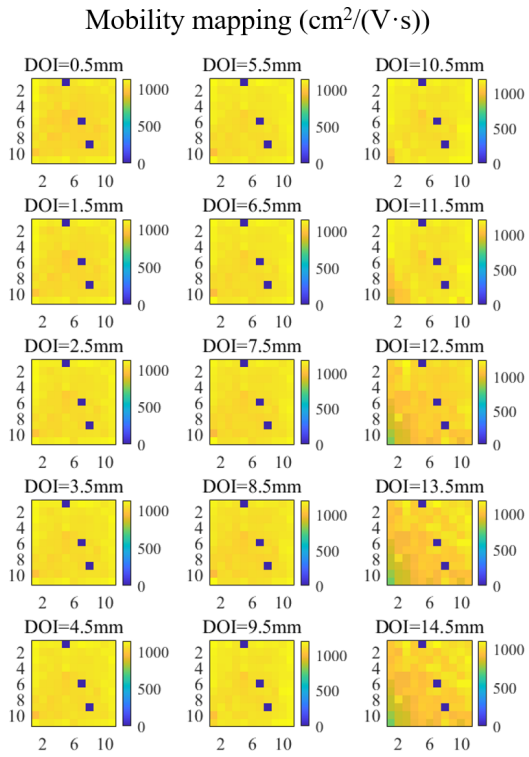

Fig. 14. 3-D electron mobility of the CdZnTe detector (voxel accuracy is 2 mm × 2 mm × 1 mm).

and photoelectric effect energy spectrum with deep screening (yellow). The test energy spectrum includes the Compton effect, multiple scattering photons, etc., and these events trigger more than one anode pixel at a time. The photoelectric effect spectrum was drawn by screening events triggered by only a single pixel in the test spectrum. The depth screening spectrum screened the photoelectric effect events within the depth range of DOI = 0–8 mm based on prior experience in Fig. 11. It can be seen intuitively from Fig. 12 that just screening photoelectric effect events can significantly reduce the Compton plateau and increase the peak-to-Compton ratio (PCR). Further screening based on DOI can effectively improve the energy resolution of the detector. The calculation shows that for the test energy spectrum, the photoelectric effect spectrum, and the depth-screened photoelectric effect spectrum, the PCR is 5.64, 11.35, and 14.55, respectively, and the energy resolution enhancement for the photoelectric effect and depth screening is 0.2% and 14.2%, respectively.

B. Calculation of Carrier Mobility Based on the DOI

In most cases, the carrier mobility μ is a fixed value in the crystal. Combining the DOI and the rising time of the induced signal on the charge-sensitive preamplifier, the mobility at different depths and voxels in the CdZnTe bulk crystal can be further calculated. The carrier mobility can be calculated by the following equation:

$$\mu = \frac{d_{\text{drift}}}{t \cdot E} = \frac{D \cdot d_{\text{drift}}}{t \cdot V}. \tag{7}$$

Among them, t is the drift time of the carriers, D is the detector thickness, V is the applied bias on the cathode, and d_{drift} is the drifting distance of the carriers, which equals $D -$ DOI for electrons and DOI for holes. The ^{137}Cs incidents from the cathode and collects the induction signal of the cathode and anode together with the rise time of the anode signal. Because of ignoring the effect of the short drifting distance of the holes here, the mobility calculated by (7) is regarded as electron mobility.

TABLE I
MEASURED MOBILITY IN CDZNTE DETECTOR

Detector size (mm × mm × mm)	Anode structure	Electron Mobility ($\frac{cm^2}{V \cdot s}$)	Reference
22 × 22 × 15	Pixel	1000-1150	Present work
10 × 10 × 10	Pixel	1000	[20]
5.9 × 5.9 × 5	Pixel	906.4	[21]
10 × 10 × 10	Coplanar grid	1379±114	[22]
10 × 10 × 5	Plane	1118-1173	[19]
5 × 5 × 1	Plane	1050	[23]
9.3 × 8.2 × 5.1	Plane	968	[24]
5 × 5 × 1	Plane	960-1100	[25]
10 × 10 × 10	-	990.9-1312.5	[26]
5 × 5 × 1.8	-	1148	[27]

Among all the detector pixels, three pixels with high noise levels are disabled during the test. The positions of the disabled pixels are dark blue squares in the subimages of Fig. 14. From Figs. 13 and 14, the electron mobility of the CdZnTe crystal is about 1000–1150 cm^2/(V·s), and the electron mobility fluctuates in a small range in different regions of the crystal. This result is consistent with the results obtained by our group in previous experimental tests [19]. Table I shows the comparison of the electron mobility obtained by our calculation and the experimental results tested by other research groups. The calculated electron mobility is within the range of experimental results, which also proves the high reliability of the calculation. After DOI > 11 mm, the calculated mobility decreases at the lower left corner of the detector, and there

is a slight decrease at the upper right of the detector. It is speculated that the defect density of the single crystal in the lower left part close to anode may be higher than that of other detector regions. The trapping or scattering here is severe, which deteriorates the carrier transport performance. Based on the DOI and drifting time, the electron mobility can be directly calculated, and at the same time the crystal defects' existence can be preliminarily judged.

V. Conclusion

This article calibrated the relationship between the DOI and the ratio of cathode and anode signals for thick CdZnTe detectors using high-energy ray sources. The calibration experiment showed a strong linear relationship, and the optimal fitting parameters were obtained. The linear calibration means signal analysis can be simpler and faster for nuclear medicine and industrial applications. The energy spectrum was drawn based on DOI analysis by screening the photoelectric effect signals within the depths with high energy resolution and characteristic peak position. The CdZnTe detector achieves an energy resolution of 0.707% for ^{137}Cs@662 keV of a 14.2% improvement and increases the PCR from 5.64 to 14.55. This screening method provides technical support for precise nuclide identification applications. Based on the DOI and drifting time, the 2-D and 3-D electron mobility of the CdZnTe crystal was calculated, which is almost within the range of 1000–1150 $cm^2/(V{\cdot}s)$. This delivers a new method for direct mobility testing. Mobility mapping may provide a new roadmap for crystal defeats evaluation for bulk single-crystal semiconductors.

Acknowledgment

The authors would like to thank the Northwest Institute of Nuclear Technology, Shaanxi Weifeng Nuclear Electronics Company, Ltd., and Imdetek Company, Ltd., for their experiment support.

References

[1] B. D. Milbrath, A. J. Peurrung, M. Bliss, and W. J. Weber, "Radiation detector materials: An overview," *J. Mater. Res.*, vol. 23, no. 10, pp. 2561–2581, Oct. 2008.

[2] Y. Eisen, "CdTe and CdZnTe materials for room-temperature X-ray and gamma ray detectors," *J. Cryst. Growth*, vols. 184–185, nos. 1–2, pp. 1302–1312, Feb. 1998.

[3] S. Del Sordo, L. Abbene, E. Caroli, A. M. Mancini, A. Zappettini, and P. Ubertini, "Progress in the development of CdTe and CdZnTe semiconductor radiation detectors for astrophysical and medical applications," *Sensors*, vol. 9, pp. 3491–3526, Sep. 2009.

[4] L. Verger *et al.*, "Performance and perspectives of a CdZnTe-based gamma camera for medical imaging," *IEEE Trans. Nucl. Sci.*, vol. 51, no. 6, pp. 3111–3117, Dec. 2004.

[5] D. Matsuura, K. Genba, Y. Kuroda, H. Ikebuchi, and T. Tomonaka, "'ASTROCAM 7000HS' radioactive substance visualization camera," *Mitsubishi Heavy Industries Tech. Rev.*, vol. 51, no. 1, pp. 68–75, 2014.

[6] F. P. Doty *et al.*, "Pixellated CdZnTe detector arrays," *Nucl. Instrum. Methods Phys. Res. A, Accel. Spectrom. Detect. Assoc. Equip.*, vol. 353, nos. 1–3, pp. 356–360, Dec. 1994.

[7] Z. He, G. F. Knoll, D. K. Wehe, and Y. F. Du, "Coplanar grid patterns and their effect on energy resolution of CdZnTe detectors," *Nucl. Instrum. Methods Phys. Res. A, Accel. Spectrom. Detect. Assoc. Equip.*, vol. 411, pp. 107–113, Jul. 1998.

[8] G. Montemont, M. Arques, L. Verger, and J. Rustique, "A capacitive Frisch grid structure for CdZnTe detectors," *IEEE Trans. Nucl. Sci.*, vol. 48, no. 3, pp. 278–281, Jun. 2001.

[9] Z. He, W. Li, G. F. Knoll, D. K. Wehe, J. Berry, and C. M. Stahle, "3-D position sensitive CdZnTe gamma-ray spectrometers," *Nucl. Instrum. Methods Phys. Res. A, Accel. Spectrom. Detect. Assoc. Equip.*, vol. 422, nos. 1–3, pp. 173–178, 1999.

[10] Y. D. Ma, S. L. Xiao, G. Q. Yang, and L. Q. Zhang, "Investigation of a CPG-array CdZnTe γ-ray imaging detector with single collecting electrodes readout," *J. Synchrotron Radiat.*, vol. 22, pp. 1403–1409, Nov. 2015.

[11] A. E. Bolotnikov *et al.*, "A 4×4 array module of position-sensitive virtual Frisch-grid CdZnTe detectors for gamma-ray imaging spectrometers," *Nucl. Instrum. Methods Phys. Res. A, Accel. Spectrom. Detect. Assoc. Equip.*, vol. 954, Feb. 2020, Art. no. 161036.

[12] Z. He, W. Li, G. F. Knoll, D. K. Wehe, and C. M. Stahle, "Measurement of material uniformity using 3-D position sensitive CdZnTe gamma-ray spectrometers," *Nucl. Instrum. Methods Phys. Res. A, Accel. Spectrom. Detect. Assoc. Equip.*, vol. 441, no. 3, pp. 459–467, Mar. 2000.

[13] Z. He, "Review of the Shockley–Ramo theorem and its application in semiconductor gamma-ray detectors," *Nucl. Instrum. Methods Phys. Res. A, Accel. Spectrom. Detect. Assoc. Equip.*, vol. 463, nos. 1–2, pp. 250–267, May 2001.

[14] F. Zhang, Z. He, and D. Xu, "Analysis of detector response using 3-D position-sensitive CZT gamma-ray spectrometers," *IEEE Trans. Nucl. Sci.*, vol. 51, no. 6, pp. 3098–3104, Dec. 2004.

[15] Z. He, G. F. Knoll, and D. K. Wehe, "Direct measurement of product of the electron mobility and mean free drift time of CdZnTe semiconductors using position sensitive single polarity charge sensing detectors," *J. Appl. Phys.*, vol. 84, no. 10, pp. 5566–5569, Nov. 1998.

[16] J. Carrascal *et al.*, "Energy and DOI calibrations for high spatial resolution CZT detectors," *IEEE Trans. Nucl. Sci.*, vol. 61, no. 1, pp. 518–527, Feb. 2014.

[17] F. Mathy *et al.*, "A three-dimensional model of CdZnTe gamma-ray detector and its experimental validation," *IEEE Trans. Nucl. Sci.*, vol. 51, no. 5, pp. 2419–2426, Oct. 2004.

[18] L. Verger *et al.*, "Characterization of CdTe and CdZnTe detectors for gamma-ray imaging applications," *Nucl. Instrum. Methods Phys. Res. A, Accel. Spectrom. Detect. Assoc. Equip.*, vol. 458, nos. 1–2, pp. 297–309, Feb. 2001.

[19] F. Yang, W. Jie, G. Zha, S. Xi, M. Wang, and T. Wang, "The effect of indium doping on deep level defects and electrical properties of CdZnTe," *J. Electron. Mater.*, vol. 49, no. 2, pp. 1243–1248, Feb. 2020.

[20] W. Li, Z. He, G. F. Knoll, D. K. Wehe, and Y. F. Du, "A modeling method to calibrate the interaction depth in 3-D position sensitive CdZnTe gamma-ray spectrometers," *IEEE Trans. Nucl. Sci.*, vol. 47, no. 3, pp. 890–894, Jun. 2000.

[21] H. Y. Cho, J. H. Lee, Y. K. Kwon, J. Y. Moon, and C. S. Lee, "Measurement of the drift mobilities and the mobility-lifetime products of charge carriers in a CdZnTe crystal by using a transient pulse technique," *J. Instrum.*, vol. 6, no. 1, Jan. 2011, Art. no. C01025.

[22] H. Yücel, Ö. Birgül, E. Uyar, and Ş. Çubukçu, "A novel approach in voltage transient technique for the measurement of electron mobility and mobility-lifetime product in CdZnTe detectors," *Nucl. Eng. Technol.*, vol. 51, no. 3, pp. 731–737, Jun. 2019.

[23] K. Suzuki, T. Sawada, and K. Imai, "Effect of DC bias field on the Time-of-flight current waveforms of CdTe and CdZnTe detectors," *IEEE Trans. Nucl. Sci.*, vol. 58, no. 4, pp. 1958–1963, Aug. 2011.

[24] U. N. Roy, S. Weiler, J. Stein, M. Groza, V. Buliga, and A. Burger, "Charge transport properties of as-grown CZT by traveling heater method," *Nucl. Instrum. Methods Phys. Res. A, Accel. Spectrom. Detect. Assoc. Equip.*, vol. 652, no. 1, pp. 162–165, Oct. 2011.

[25] K. Suzuki, S. Seto, T. Sawada, and K. Imai, "Carrier transport properties of HPB CdZnTe and THM CdTe:Cl," *IEEE Trans. Nucl. Sci.*, vol. 49, no. 3, pp. 1287–1291, Jun. 2002.

[26] W. Mengesha, C. E. Aalseth, D. S. Barnett, M. Bliss, and C. Schaefer, "Pulse shape analysis for electron mobility study in cadmium zinc telluride gamma-ray detectors," in *Proc. IEEE Nucl. Sci. Symp. Conf. Rec.*, Portland, OR, USA, Oct. 2004, pp. 3498–3502.

[27] T. Wang *et al.*, "Study on a co-doped CdZnTe crystal containing Yb and In," *CrystEngComm*, vol. 21, no. 16, pp. 2620–2625, Apr. 2019.